

Nonlinear force-free coronal magnetic field modeling scheme based on the direct boundary integral formulation

Han He,^{1,2} and Huaning Wang¹

Abstract. The boundary integral equation (BIE) method was first proposed by Yan and Sakurai [2000], which is used to extrapolate the nonlinear force-free magnetic field in the solar atmosphere. Recently, Yan and Li [2006] improved the BIE method and proposed the direct boundary integral equation (DBIE) formulation, which represents the nonlinear force-free magnetic field by direct integration of the magnetic field on the bottom boundary surface. Based on this new method, we devised a practical calculation scheme for the nonlinear force-free field modeling above solar active regions. The code of the scheme was tested both by the analytical solutions given by Low and Lou [1990], and by the observed data of vector magnetograms in the photosphere. The calculated field lines above the active regions present the X-shaped structure as well as the S-shaped loops, which can be helpful for understanding the magnetic reconnection processes during solar flares.

1. Introduction

Both observations and theoretical analyses revealed that magnetic field plays an important role in the activity phenomena of solar atmosphere: moving plasma are confined to magnetic field lines, and magnetic field also provides the energy for solar flares and other eruptive phenomena [Masuda et al., 1994; Shibata et al., 1995; Tsuneta, 1996; Priest and Forbes, 2002; Lin et al., 2005; Schwenn, 2006]. To understand the physical mechanisms of these activities in the solar atmosphere, an important step is to find out the underlying structure of the magnetic field above the related active region. Currently, the direct measurement of the magnetic field in the solar chromosphere and corona is not as sophisticated as the observation in the photosphere. The commonly used method to understand the configurations of the magnetic fields above the photosphere is extrapolation: the fields can be reconstructed from a physical model in which the observed photospheric magnetic field is taken as a boundary condition. The force-free field model is often adopted for this purpose, since it is a reasonable approximation in the solar chromosphere and corona [Metcalf et al., 1995].

The nonlinear force-free magnetic field, with the field lines being everywhere aligned parallel to the electric current density, can be described by equations:

$$(\nabla \times \mathbf{B}) \times \mathbf{B} = 0, \quad (1)$$

$$\nabla \cdot \mathbf{B} = 0. \quad (2)$$

Equation (2) is the divergence-free constraint of the magnetic field. The force-free constraint (1) can also be written as

$$\nabla \times \mathbf{B} = \alpha(\mathbf{r})\mathbf{B}, \quad (3)$$

where α is a function of spatial location, usually called the force-free parameter or force-free factor. It is constant along

each field line, which can be determined from the bottom boundary condition.

Currently, several methods for nonlinear force-free field modeling have been proposed [Sakurai, 1981; Yan and Sakurai, 2000; Wheatland et al., 2000; Wiegmann, 2004; Régnier and Amari, 2004; Valori et al., 2005; Yan, 2005; Wiegmann et al., 2006; Yan and Li, 2006; Amari et al., 2006; Wheatland, 2006; Song et al., 2006; Schrijver et al., 2006]. As one of the techniques for nonlinear force-free field extrapolation, the boundary integral equation (BIE) method was first proposed by Yan and Sakurai [2000]. Recently, Yan and Li [2006] improved the BIE and proposed the direct boundary integral equation (DBIE) formulation, which represents the force-free magnetic field by direct integration of the magnetic field on the bottom boundary surface. Figure 1 shows the geometry for application of DBIE [Yan and Li, 2006]. On the bottom boundary surface Γ (infinite plane), the boundary condition is

$$\mathbf{B} = \mathbf{B}_0 \text{ on } \Gamma, \quad (4)$$

where \mathbf{B}_0 denotes the known boundary values which can be supplied from vector magnetogram measurements. At infinity, an asymptotic constraint condition is also introduced to ensure a finite energy content in the semispace Ω above Γ ,

$$\mathbf{B} = O(r^{-2}) \text{ when } r \rightarrow \infty, \quad (5)$$

where r is radial distance.

According to the DBIE method, after a series of derivations by using the two constraint conditions (2)-(3) and the two boundary conditions (4)-(5), the magnetic strength at the field point (x_i, y_i, z_i) in Ω can be represented by equation [Yan and Li, 2006]:

$$\mathbf{B}_i = - \int_{\Gamma} \frac{\partial Y}{\partial n} \mathbf{B}_0 d\Gamma = \int_{\Gamma} \frac{\partial Y}{\partial z} \mathbf{B}_0 d\Gamma. \quad (6)$$

The reference function Y in equation (6) is chosen as

$$Y = \frac{\cos(\lambda\rho)}{4\pi\rho} - \frac{\cos(\lambda\rho')}{4\pi\rho'}, \quad (7)$$

where $\rho = [(x - x_i)^2 + (y - y_i)^2 + (z - z_i)^2]^{1/2}$ is the distance between a variable point (x, y, z) and the given field point (x_i, y_i, z_i) , $\rho' = [(x - x_i)^2 + (y - y_i)^2 + (z + z_i)^2]^{1/2}$, as shown in Figure 1. The parameter λ in equation (7) has the same

¹National Astronomical Observatories, Chinese Academy of Sciences, Beijing, China.

²Kwasan and Hida Observatories, Graduate School of Science, Kyoto University, Kyoto, Japan.

dimension (reciprocal of length) as the force-free factor α , which is defined by equation

$$\int_{\Omega} Y (\lambda^2 \mathbf{B} - \alpha^2 \mathbf{B} - \nabla \alpha \times \mathbf{B}) d\Omega = 0. \quad (8)$$

In the case of nonlinear force-free field, corresponding to B_{ix} , B_{iy} , and B_{iz} in equation (6), there exist three components of the reference function, Y_x , Y_y , and Y_z , together with λ_x , λ_y , and λ_z defined locally at the given field point by equation (8). The values of the three components of λ are generally different [Li et al., 2004; Yan and Li, 2006; He and Wang, 2006].

Once the parameter λ_x , λ_y , and λ_z at the field point (x_i, y_i, z_i) are given, the magnetic field \mathbf{B}_i can be calculated by integration of the magnetic field on the bottom boundary surface through the DBIE formulation (6). Because it is costly to determine λ directly from the volume integral equation (8), Yan and Li [2006] devised an optimal approach to find the suitable λ values locally by using the DBIE (6) together with the force-free constraint condition (1). At the field point (x_i, y_i, z_i) , they defined an evaluate function as:

$$f_i(\lambda_x, \lambda_y, \lambda_z) = \frac{|\mathbf{J} \times \mathbf{B}|}{|\mathbf{J}||\mathbf{B}|}, \quad \text{with } \mathbf{J} = \nabla \times \mathbf{B}, \quad (9)$$

which measures the absolute value of sine of the angle between \mathbf{J} and \mathbf{B} . For any initial values of λ_x , λ_y , and λ_z , \mathbf{B} at the field point and its neighborhood can be calculated by DBIE (6), then the value of $f_i(\lambda_x, \lambda_y, \lambda_z)$ can be obtained by equation (9). In ideal situation, the suitable λ values (denoted by λ_x^* , λ_y^* , and λ_z^*) can be determined by

$$f_i(\lambda_x^*, \lambda_y^*, \lambda_z^*) = 0, \quad (10)$$

which is equivalent to the force-free field equation (1). In practical computing, one needs to find $(\lambda_x^*, \lambda_y^*, \lambda_z^*)$ that satisfies

$$f_i(\lambda_x^*, \lambda_y^*, \lambda_z^*) = \min f_i(\lambda_x, \lambda_y, \lambda_z). \quad (11)$$

A downhill simplex method can be employed to fulfil the task of equation (11) [Nelder and Mead, 1965; Yan and Li, 2006]. The computation of Yan and Li [2006] shows that, if the equation (10) is satisfied, the divergence-free constraint (2) can also be satisfied at the neighborhood of the given

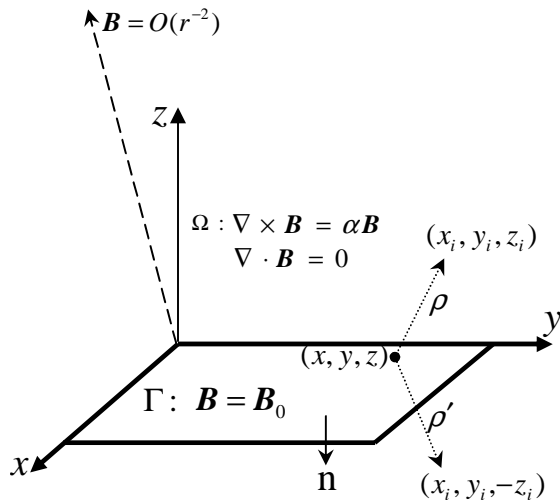


Figure 1. The geometry for application of the direct boundary integral equation (DBIE).

field point. This property indicates that the divergence-free constraint (2) has been involved during the derivation of the DBIE formulation (6).

We followed the main idea of the strategy proposed by Yan and Li [2006], and devised the upward boundary integration scheme for nonlinear force-free field modeling. That is, while we take into account the whole boundary data information through the DBIE formulation (6), the parameter λ at a given field point can be determined locally through the force-free equation (1) or equation (10) with the help of only neighboring boundary data information. Unlike the original procedure of Yan and Li [2006], our computation is carried out layer by layer upwardly. The procedure and techniques of the new scheme is described in section 2. The code of the scheme was tested by the analytical solutions given by Low and Lou [1990], as well as the observed vector magnetograms of solar active regions in the photosphere. The results of the test calculations are presented in section 3. In section 4, we give the summary and discussion.

2. Upward Boundary Integration Scheme

In the original computational procedure proposed by Yan and Li [2006], the equation (11) has better convergence property at field point with lower altitude. To take advantage of this property and avoid the increasing error at field point

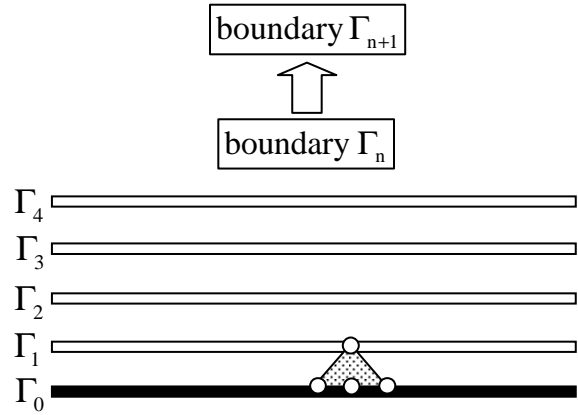


Figure 2. The diagram to illustrate the upward boundary integration scheme for nonlinear force-free field modeling based on the DBIE formulation (6). The computation is carried out layer by layer upwardly, the field distribution at Γ_{n+1} is calculated from the data of Γ_n .

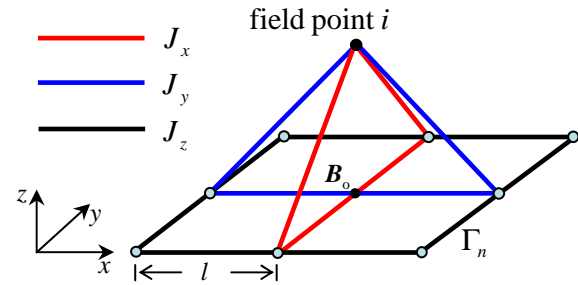


Figure 3. The diagram to illustrate the calculation of $\mathbf{J}(\sim \nabla \times \mathbf{B})$ in the small square pyramid between the field point i and the neighboring grid points at Γ_n . The height of the square pyramid is l and the side length of the square base is $2l$, where l denotes the space between two consecutive grid points at Γ_n . J_x and J_y are calculated in two isosceles triangles respectively, J_z is calculated in the square base of the pyramid.

with higher altitude, we devised a new scheme for nonlinear force-free field modeling based on the DBIE formulation (6), which we called the upward boundary integration scheme.

In the new scheme, as shown in Figure 2, the computation is carried out layer by layer upwardly, from Γ_0 (photosphere) to Γ_1 , then Γ_1 to Γ_2 , and so on. In the original procedure of Yan and Li [2006], the bottom boundary was fixed to the photosphere, while in our scheme, the bottom boundary for applying the DBIE formulation (6) is moved upwardly layer by layer. That is, we always calculate the field distribution at Γ_{n+1} from the data of the new bottom boundary Γ_n . The step distance between the two consecutive layers is the same as the space between the two consecutive grid points at Γ_n (the scale of one pixel). Since Γ_{n+1} is very close to Γ_n , the field points at Γ_{n+1} are always at very low altitude relative to the bottom boundary Γ_n , then the equation (11) can achieve fine convergence property at every layer.

In the original procedure of Yan and Li [2006], the values of f_i and \mathbf{J} in equation (9) are calculated in the infinitesimal neighborhood $\pm\delta$ of the field point in x-, y-, and z-directions (small cubic volume surrounding the field point). The computing of the integration in DBIE formulation (6) should be done seven times (six sides of the small cube plus the field point itself) to obtain the value of f_i and \mathbf{J} . To reduce the loads of computing and fully utilize the boundary data information at Γ_n , in our scheme, we calculate f_i and \mathbf{J} in a small square pyramid between the field point i and the neighboring grid points at the boundary Γ_n , as shown in Figure 3.

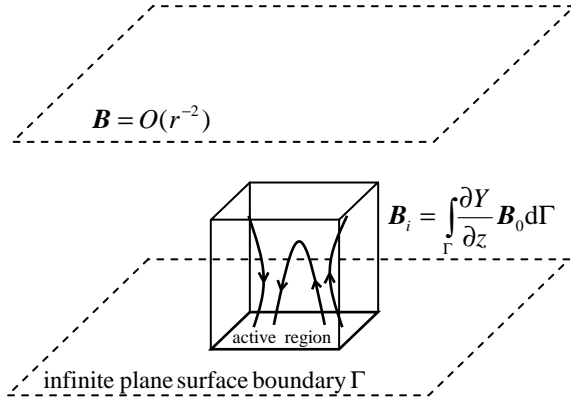


Figure 4. The diagram to illustrate the application of the DBIE to an isolated active region. The observed boundary data of the active region are bounded in a finite square area. The field out of the square area at boundary Γ is considered to be zero. The cubic volume above the square boundary data area represents the output region of the code.

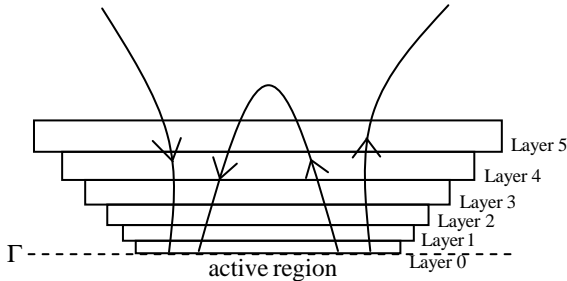


Figure 5. The diagram to illustrate how to fit expanding field at higher layers. The square area for the integration of the DBIE is enlarged gradually layer by layer. The pixel number of the square areas is fixed by resampling the grid points at all layers to save the computing time.

The height of the pyramid is l (distance between Γ_{n+1} and Γ_n) and the side length of the square base is $2l$, where l denotes the space between two consecutive grid points at Γ_n (the scale of one pixel). Given an arbitrary λ at field point i , to obtain the values of $f_i(\lambda)$ and $\mathbf{J}(\lambda)$ in equation (9), we only need to carry out the integration of DBIE (6) one time at the field point i to calculate $\mathbf{B}_i(\lambda)$, thus save the computing time as compared with the original procedure of Yan and Li [2006]. Once $\mathbf{B}_i(\lambda)$ is known, J_x , J_y , and J_z can be calculated in two isosceles triangles and the square base of the pyramid respectively as indicated by different colors in Figure 3. \mathbf{B}_0 at the center of the square base, as shown in Figure 3, is employed to complete the calculation of $f_i(\lambda)$. Then we can use equation (11) to find the suitable value of λ^* . Once λ^* is determined, $\mathbf{B}_i(\lambda^*)$ will be the final result at the field point i for the nonlinear force-free field modeling.

As described in section 1, the DBIE formulation (6) demands the bottom boundary Γ to be an infinite plane surface [Yan and Li, 2006]. Figure 4 illustrates how to apply the DBIE to an isolated active region. At the bottom boundary Γ , the observed boundary data of the active region are bounded in a finite square area. Out of the square area, the field at Γ can be considered to be zero. Then, in practical calculation, we only need to carry out the integration of DBIE (6) over the finite square area of the active region, while the bottom boundary Γ is still an infinite plane surface.

Considering the magnetic field may expand at higher layers, the square area for the integration is enlarged gradually layer by layer during the calculation (in present code, from Γ_n to Γ_{n+1} , each side of the square area expands one pixel), as illustrated in Figure 5. Meanwhile, we keep the original pixel number of the square area by resampling the grid points at all layers to save the computing time. Thus the space between the two consecutive grid points at Γ_n as well as the distance between the two consecutive layers also increase gradually with height, as shown in Figure 5. After

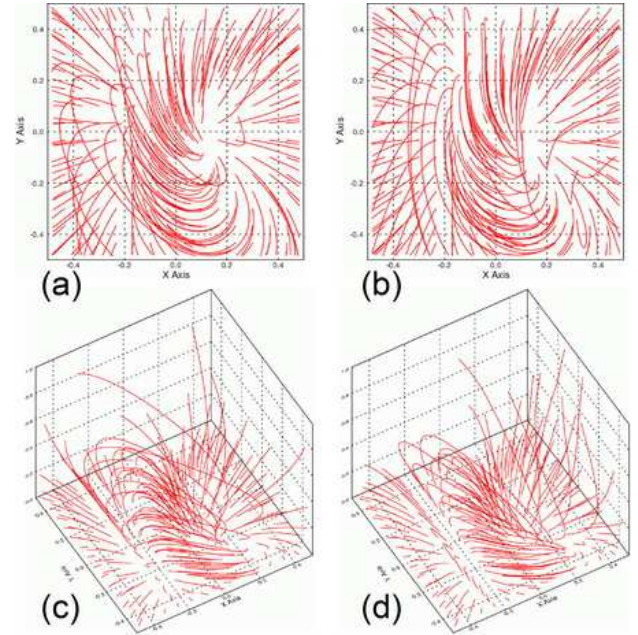


Figure 6. The extrapolated field lines for Case I compared with the theory solutions of Low and Lou [1990]. Left column (a) and (c) are images of theory solution, right column (b) and (d) are images of calculated field. Top row are images in top view, bottom row are images in 3-D view.

the field distributions at a series of layers are obtained, the values of the magnetic field at other field points between the layers and grid points can be calculated through the technique of interpolation.

In practical calculation, the code reads the boundary data (vector magnetogram observed in photosphere) of an active region (square area, $N \times N$ array in the code), calculate the nonlinear force-free field distributions at all layers, and reform the grid structure to a regular form through interpolation. The output of the code is the field distribution in a cubic volume (by a regular grid with $N \times N \times N$ array in the code) which is just above the boundary data area, as illustrated in Figure 4. The current code is written in IDL programming language. The time needed for $64 \times 64 \times 64$ output grid is about 13 hours on an 1.86GHz Intel processor.

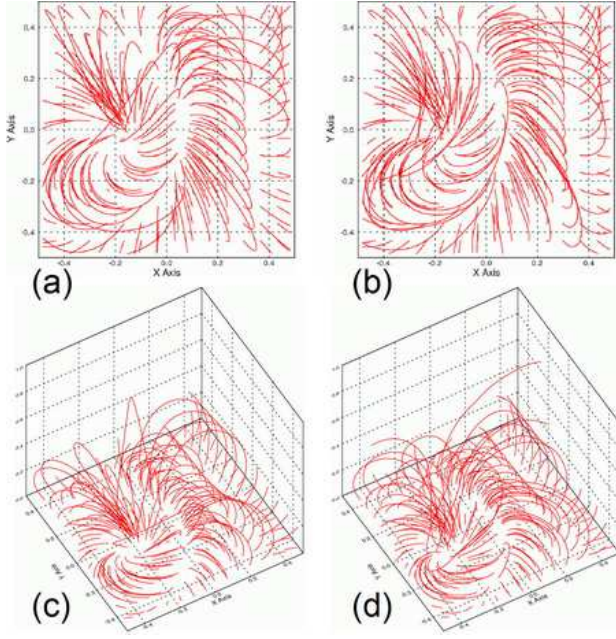


Figure 7. The extrapolated field lines for Case II compared with the theory solutions of Low and Lou [1990]. Left column (a) and (c) are images of theory solution, right column (b) and (d) are images of calculated field. Top row are images in top view, bottom row are images in 3-D view.

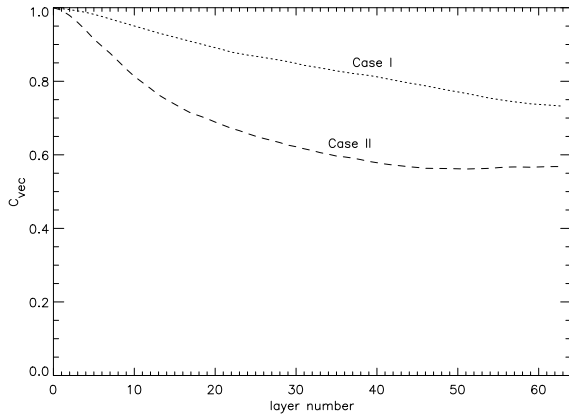


Figure 8. The curves of vector correlation metric C_{vec} (defined in equation (12)) vs height for Case I and Case II in section 3.1. C_{vec} is calculated at each layer in the central domain $x, y \in [-0.5, +0.5]$ and $z \in [0, 2]$, with $32 \times 32 \times 64$ grid.

3. Results of Test Calculations

3.1. Low and Lou Analytical Solutions

Firstly, we test our code by the analytical nonlinear force-free field solutions given by Low and Lou [1990]. The fields of the analytical solutions are basically axially symmetric. The point source of the axisymmetric fields is located at the origin of the spherical coordinate system, with the axis of symmetry pointing to z direction. By arbitrarily positioning the plane surface boundary Γ of DBIE in the space of the analytical fields, we can get different kind of boundary conditions prepared for extrapolation. Two cases are selected to test the validity and accuracy of our code, which are the same cases as used by Schrijver et al. [2006]. The parameters for Case I are $n = 1, m = 1, L = 0.3, \Phi = \pi/4$, the parameters for Case II are $n = 3, m = 1, L = 0.3, \Phi = 4\pi/5$, where n and m are the eigenvalues of the solutions, L is the distance between the boundary surface Γ and the point source (origin of the spherical coordinate system), and Φ is the angle between the normal direction of Γ and the z axis of the spherical coordinate system. In both cases, we calculate the field distribution in a cubic volume bounded by $x, y \in [-1, +1]$ and $z \in [0, 2]$ (x, y , and z are Cartesian coordinates defined locally on the boundary surface Γ), just as described in section 2 and illustrated in Figure 4. The pixel numbers of the boundary data are 64×64 .

The extrapolated field lines for Case I and Case II are compared with the theory solutions in Figure 6 and Figure

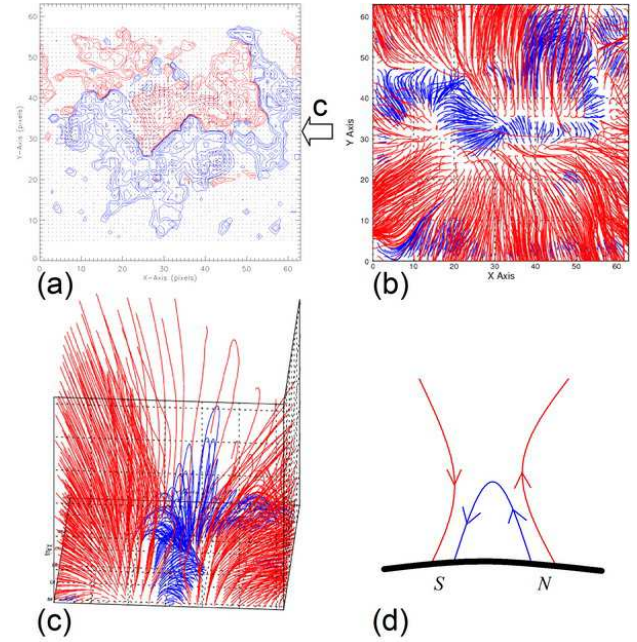


Figure 9. Results of the field modeling for active region NOAA 9077. (a) The vector magnetogram used by the code. Red contours represent positive polarity of B_z , blue contours represent negative polarity of B_z , small arrows overlaying the contours represent B_t (transverse component). The data was observed at 04:14 UT on 14 July 2000 by the Solar Multi-Channel Telescope (SMCT) at Huairou Solar Observing Station. The field of view is $269'' \times 269''$ with pixel number as 64×64 ($4.2''/\text{pix}$). (b) Top view of the extrapolated field. Closed field lines are plotted in blue color, open field lines are in red color. (c) Side view of the extrapolated field along the direction of the neutral line as indicated by an arrow in the right margin of Figure 9a. (d) Diagram to illustrate the X-shaped structure of the field lines.

7 respectively. Left columns are images of theory solutions, right columns are images of calculated fields. Figure 6 and Figure 7 only show the central domain ($x, y \in [-0.5, +0.5]$ and $z \in [0, 1]$, with $32 \times 32 \times 32$ grid) of the modeling volume, where the quality of agreement between the extrapolated field and the theory solutions is better than in the margin area.

A vector correlation metric C_{vec} is employed to quantify the degree of agreement between the theory field \mathbf{B} and the extrapolated field \mathbf{b} as used by Schrijver et al. [2006]. C_{vec} is defined as

$$C_{\text{vec}} \equiv \frac{\sum \mathbf{B}_i \cdot \mathbf{b}_i}{\left(\sum |\mathbf{B}_i|^2 \sum |\mathbf{b}_i|^2\right)^{1/2}}, \quad (12)$$

where \mathbf{B}_i and \mathbf{b}_i are the field vectors at each grid point i . If \mathbf{B} and \mathbf{b} are identical, $C_{\text{vec}} = 1$; if $\mathbf{B}_i \perp \mathbf{b}_i$, $C_{\text{vec}} = 0$. We calculated the values of C_{vec} at each layer in the central domain ($x, y \in [-0.5, +0.5]$ and $z \in [0, 2]$, with $32 \times 32 \times 64$ grid), the results are shown in Figure 8. Since we only use the finite boundary data in the domain $x, y \in [-1, +1]$ with 64×64 grid, it can be seen that the extrapolated fields \mathbf{b} deviate from the theory fields \mathbf{B} gradually with the increasing of height. At the lower layers and in the central domain, \mathbf{B}

and \mathbf{b} get the best agreement, as illustrated in Figure 6 and Figure 7.

3.2. Observed Data of Vector Magnetograms

Secondly, we test our code by observed boundary data of solar active regions. Three vector magnetograms that were obtained by three telescopes respectively are employed for this purpose.

The first vector magnetogram for testing was observed by Solar Multi-Channel Telescope (SMCT), which is located at Huairou Solar Observing Station of NAOC (National Astronomical Observatories, Chinese Academy of Sciences) in Beijing. The number of the active region is NOAA 9077. The data was observed at 04:14 UT on 14 July 2000, just several hours before the Bastille Day event (X5.7 flare) at 10:24 UT. The original field of view of the magnetogram is $313'' \times 218''$ from a 512×512 pixel size CCD. We reformed the magnetogram to a square area ($269'' \times 269''$) through cropping and interpolation, and reduced the pixel number to 64×64 ($4.2''/\text{pixel}$). The final magnetogram which is ready for the modeling calculation is shown in Figure 9a. The extrapolated field lines are shown in Figure 9b and 9c. Blue lines is closed field lines with both footpoints anchored at the bottom boundary, and red lines represent the open field lines. Figure 9b is top view, and Figure 9c is side view of the field configuration along the direction of the neutral line as indicated by an arrow in the right margin of Figure 9a. All the field lines are plotted from Γ_1 to avoid the influences of noises in the data of Γ_0 (photosphere). In Figure

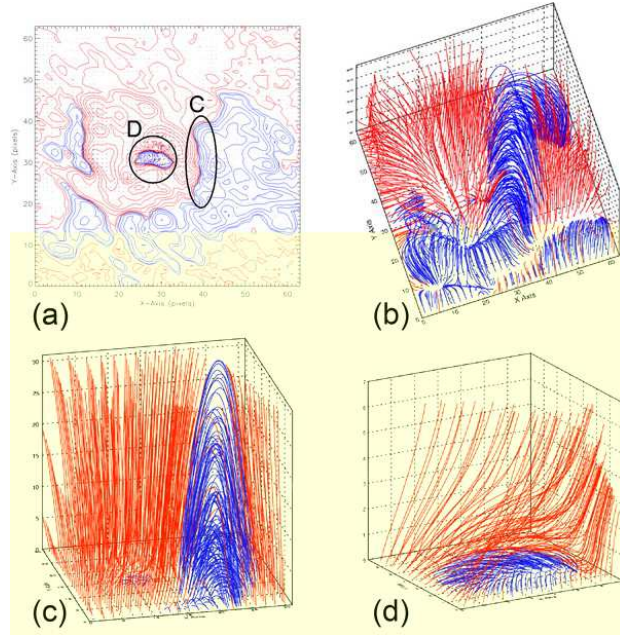


Figure 10. Results of the field modeling for active region NOAA 10808. (a) The vector magnetogram used by the code. Red contours represent positive polarity of B_z , blue contours represent negative polarity of B_z , small arrows overlaying the contours represent B_t (transverse component). The data was observed at 22:43 UT on 11 September 2005 by the Solar Magnetic Activity Research Telescope (SMART) at Hida Observatory. The field of view is $299'' \times 299''$ with pixel number as 64×64 ($4.67''/\text{pixe}$). (b) 3-D view of the extrapolated field. Closed field lines are plotted in blue color, open field lines are in red color. (c) Detailed structure above the local region marked by “C” in Figure 10a. (d) Detailed structure above the local region marked by “D” in Figure 10a.

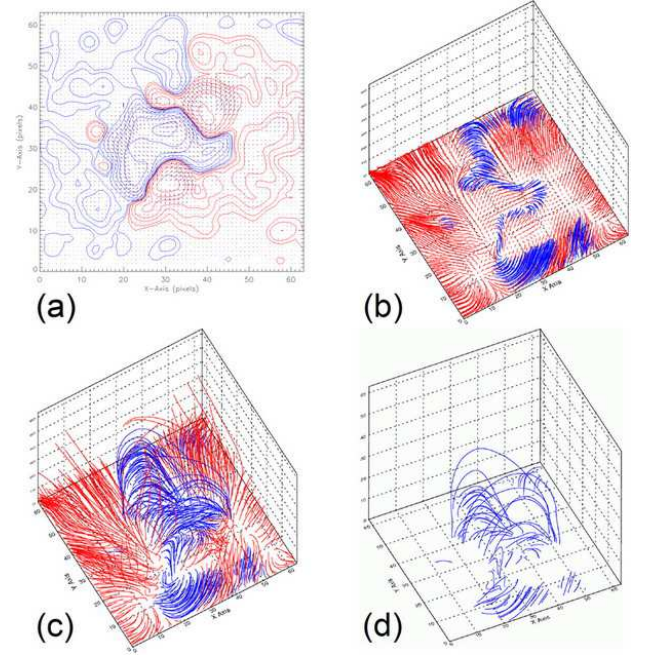


Figure 11. Results of the field modeling for active region NOAA 10484. (a) The vector magnetogram used by the code. Red contours represent positive polarity of B_z , blue contours represent negative polarity of B_z , small arrows overlaying the contours represent B_t (transverse component). The data was observed at 23:34 UT on 23 October 2003 by Solar Flare Telescope (SFT) at the Mitaka campus of NAOJ. The field of view is $340'' \times 340''$ with pixel number as 64×64 ($5.3''/\text{pixe}$). (b) Field lines at the very low layers. Closed field lines are in blue color, open field lines are in red color. (c) 3-D view of the extrapolated field. (d) 3-D view of the closed field lines. Fewer Field lines are plotted in Figure 11d than in Figure 11c to make the shapes of the field lines more clear.

9b and 9c, we can see the compact loops with different orientations aligned over the neutral line, just as the compact loops observed by TRACE (Transition Region And Coronal Explorer) satellite during the X5.7 flare of the Bastille Day event. The open field lines together with the underlying compact loops present a X-shaped structure as sketched in Figure 9d, which may imply the site of the magnetic field reconnection for the impulsive flare with compact loops [Masuda et al., 1994; Shibata et al., 1995; Priest and Forbes, 2002].

The second vector magnetogram came from the Solar Magnetic Activity Research Telescope (SMART), which is located at Hida Observatory of Kyoto University. The number of the active region is NOAA 10808. The time of the observation is 22:43 UT on 11 September 2005. We cropped a square area covering the active region NOAA 10808 from the original full-disk magnetogram obtained by SMART, and reduced the pixel number to 64×64 . The final magnetogram prepared for modeling calculation is shown in Figure 10a, the field of view is $299'' \times 299''$ with $4.67''/\text{pixel}$. The extrapolated field lines are displayed in Figure 10b, 10c, and 10d. Also, the closed field lines are plotted in blue color, and the open field lines are in red color. Figure 10b gives the total 3-D view the field configuration, Figure 10c and 10d illustrate detailed structures of two local regions as indicated by two circles in Figure 10a. In the region marked by “C”, we can see high arcades configuration above the neutral line, while in the region “D” with isolated negative polarity, the closed field lines are constrained at the very low layers.

The third vector magnetogram used to test the code is the observation of the Solar Flare Telescope (SFT), which is located at the Mitaka campus of NAOJ (National Astronomical Observatory of Japan). The number of the active region is NOAA 10484. The vector magnetogram was obtained at 23:34 UT on 23 October 2003. The original field of view of the magnetogram is $340'' \times 320''$ with 256×240 pixels. We reform the field of view to $340'' \times 340''$ (square area) through interpolation, and then reduce the pixel number to 64×64 ($5.3''/\text{pixel}$). The final magnetogram used by the code is shown in Figure 11a. Figure 11b, 11c, and 11d present the results of the extrapolation. Closed field lines are in blue color, and open field lines are in red color. Figure 11b shows the field lines at the very low layers. We can see the high-sheared compact loops aligned along the neutral line. Figure 11c gives the total 3-D view of the field configuration, and Figure 11d only illustrates the closed field lines. Fewer field lines are plotted in Figure 11d than in Figure 11c to make the shapes of the field lines more clear. It can be found that the orientations of higher loops is different than the orientations of lower arcades, also many field lines in the central domain are in S-shaped structure because of the strong-sheared field distribution in the photosphere.

4. Summary and Discussion

Based on DBIE formulation (6), we devised the upward boundary integration scheme for the nonlinear force-free field modeling. In this scheme, the computation is carried out layer by layer upwardly as shown in Figure 2. While we take into account the whole bottom boundary data information at Γ_n through the DBIE formulation (6), the suitable value of parameter λ at a given field point at Γ_{n+1} can be determined locally through the force-free constraint condition (11) with the help of only neighboring boundary data information at Γ_n , as shown in Figure 2 and 3.

The main techniques in the code of the scheme include: the bottom boundary for applying the DBIE is moved upwardly layer by layer to achieve the best convergence property and accuracy, as shown in Figure 2; the parameter λ

at a given field point is calculated in a small square pyramid (sketched in Figure 3) to fully utilize the boundary data information at Γ_n , and thus save the computing time; the square area for computing the integration of DBIE (6) is enlarged gradually layer by layer to fit the expanding field, at the same time, pixel number of the square areas is fixed by resampling the grid points at all layers to save the computing time, as illustrated in Figure 5.

In some circumstances, especially in the case of $|\mathbf{J}|$ or $|\mathbf{B}|$ approaches to zero in equation (9), equation (11) may fail to achieve an convergent result. It appears as some isolated singularity points in the raw data of Γ_{n+1} , which can be eliminated by smoothing processes with the help of nearest grid points in x-, and y- direction.

We employed the same code of downhill simplex method as used by Yan and Li [2006] to perform multidimensional minimization of f_i in equation (11). The initial starting point of $(\lambda_x, \lambda_y, \lambda_z)$ for the downhill simplex method is selected as $(0, 0, 0)$ in our code. The characteristic length scale of λ in the downhill simplex method is specified as the maximum absolute value of force-free factor α at the boundary surface Γ_0 (photosphere), because λ and α have the same dimension (reciprocal of length) and the same order of magnitude [Li et al., 2004; Yan and Li, 2006; He and Wang, 2006]. For Case I and Case II in section 3.1 (analytical solutions), the maximum absolute values of α are 11.3 and 11.1

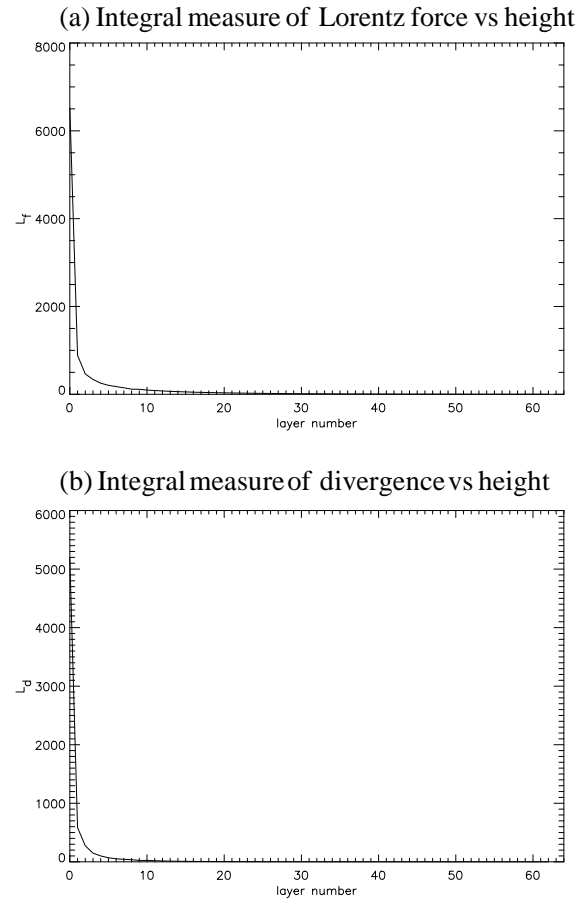


Figure 12. (a) Integral measure L_f of the Lorentz force vs height. (b) Integral measure L_d of the divergence vs height. L_f and L_d are defined in equation (13) and (14) respectively. The two curves were calculated based on the extrapolated field of NOAA 10808, as shown in Figure 10. The unit of magnetic field is Gauss and the unit of length is one pixel (~ 3405 Km).

respectively. If we adopt one pixel as the length unit (with 64×64 grid), as in our code, the values are 0.353 and 0.347. For the data of active regions observed in the photosphere, we choose the maximum possible value of α (characteristic length scale of λ) as $10 \times 10^{-8} \text{m}^{-1}$ [Pevtsov et al., 1995]. Also in our code, the length unit is one pixel, for the common active regions with field of view $300'' \times 300''$ and pixel number 64×64 , the characteristic length scale of λ becomes 0.342, which approximates to the values used for Case I and Case II of analytical solutions.

The test calculations by using the observed vector magnetograms of active regions in section 3.2 demonstrate that the DBIE formulation (6) and the upward boundary integration scheme are suitable for the nonlinear force-free field modeling above solar active regions. Only the bottom boundary data in the photosphere are needed in the calculations, and the integration over the whole boundary in DBIE formulation (6) can effectively overcome the influence of the noises in the boundary data to the convergence property of equation (11). From the corona images observed by X-Ray telescope, it can be found that the field lines above an isolated active regions are usually confined in the local area. In this situation, the code of our scheme can give fine results at higher layers, as shown in Figure 9, 10, and 11. But in the case of analytical solutions of Low and Lou [1990], the field lines present global configurations [Low and Lou, 1990; Wang and Sakurai, 1998; Li et al., 2004; He and Wang, 2006]. Because we only use the finite boundary data, the extrapolated fields and the theory solutions get the best agreement at the lower layers and in the central domain, as shown in Figure 6-8.

To check the extent to which the extrapolated fields satisfy the force-free constraint condition (1) and divergence free condition (2), we calculated the integral measure L_f of the Lorentz force and L_d of divergence of the fields, as used by Schrijver et al. [2006]. L_f and L_d are defined by equations:

$$L_f = \frac{1}{V} \int_V B^{-2} |(\nabla \times \mathbf{B}) \times \mathbf{B}|^2 dV, \quad (13)$$

$$L_d = \frac{1}{V} \int_V |\nabla \cdot \mathbf{B}|^2 dV. \quad (14)$$

We calculated L_f and L_d at each layer, Figure 12 gives a sample of the results, which is based on the second case in the section 3.2 with the vector magnetogram observed by SMART telescope as shown in Figure 10. Figure 12a is the curve of L_f vs height, and Figure 12b is the curve of L_d vs height. Both the curves show that the measures L_f and L_d decreased rapidly with the increase of height, which indicates that the force-free constraint condition (1) and divergence free condition (2) are well satisfied in the calculated field. The further and more important step to verify the reliability of the code is to compare the extrapolated field configurations with the simultaneous corona structure observations by X-Ray image telescope [Wang et al., 2000, 2001]. The data obtained by Hinode (Solar-B) satellite will be very suitable for this purpose.

The field configurations in Figure 9, 10, and 11 show some clues to the magnetic field reconnections, such as the X-shaped structure in Figure 9, the high arcades above the neutral line in Figure 10, and the sheared S-shaped loops in Figure 11, which can be helpful for understanding the magnetic reconnection processes during solar flares. Moreover, the BIE/DBIE method can be applied to the case with spherical surface boundary [Li et al., 2004; Yan, 2005; He and Wang, 2006]. By using the full disk observations of vector magnetograms, it is possible to generalize the upward boundary integration scheme to study the large scale structure of coronal magnetic field with spherical surface boundary, and its relationship with the Coronal Mass Ejections (CMEs).

Acknowledgments.

The authors thank the colleagues for valuable comments and discussions during the CAWSES International Workshop on Space Weather Modeling (CSWM) at the Earth Simulator Center in Yokohama. We thank Prof. Yihua Yan and Dr. Zhuoheng Li for helpful discussions on the principle of the BIE/DBIE method and the techniques of force-free field extrapolation. H. He greatly benefited from the deep and helpful discussions with the colleagues at Kwasan and Hida Observatories of Kyoto University. We gratefully acknowledge Huairou Solar Observing Station (Solar Multi-Channel Telescope) of NAOC, Kwasan and Hida Observatories (Solar Magnetic Activity Research Telescope) of Kyoto University, and National Astronomical Observatory of Japan (Solar Flare Telescope) for kindly permitting us to use their high quality data of vector magnetograms.

This work is supported by Projects KJCX2-YW-T04 and KG CX3-SYW-403-10 of Chinese Academy of Sciences (CAS), National Basic Research Program of China (973 Program) through grant 2006CB806307, and National Natural Science Foundation of China (NSFC) through grants 10233050 and 10673017.

References

- Amari, T., T. Z. Boulmezaoud, and J. J. Aly (2006), Well posed reconstruction of the solar coronal magnetic field, *Astron. Astrophys.*, **446**, 691–705.
- He, H., and H. N. Wang (2006), The validity of the boundary integral equation for magnetic field extrapolation in open space above a spherical surface, *Mon. Not. R. Astron. Soc.*, **369**, 207–215.
- Li, Z., Y. Yan, and G. Song (2004), Properties of the boundary integral equation for solar non-constant- α force-free magnetic fields, *Mon. Not. R. Astron. Soc.*, **347**, 1255–1265.
- Lin, J., Y.-K. Ko, L. Sui, J. C. Raymond, G. A. Stenborg, Y. Jiang, S. Zhao, S. Mancuso (2005), Direct observations of the magnetic reconnection site of an eruption on 2003 november 18, *Astrophys. J.*, **622**, 1251–1264.
- Low, B. C., and Y. Q. Lou (1990), Modeling solar force-free magnetic fields, *Astrophys. J.*, **352**, 343–352.
- Masuda, S., T. Kosugi, H. Hara, S. Tsuneta, and Y. Ogawara (1994), A loop-top hard X-ray source in a compact solar flare as evidence for magnetic reconnection, *Nature*, **371**, 495–497.
- Metcalf, T. R., L. Jiao, A. N. McClymont, R. C. Canfield, and H. Uitenbroek (1995), Is the solar chromospheric magnetic field force-free, *Astrophys. J.*, **439**, 474–481.
- Nelder, J. A., and R. Mead (1965) A simplex method for function minimization, *The Computer Journal*, **7**, 308–313.
- Pevtsov A. A., R. C. Canfield, and T. R. Metcalf (1995), Latitudinal variation of helicity of photospheric magnetic fields, *Astrophys. J.*, **440**, L109–L112.
- Priest, E. R., and T. G. Forbes (2002), The magnetic nature of solar flares, *Astron. Astrophys. Rev.*, **10**, 313–377.
- Régner, S., and T. Amari (2004), 3D magnetic configuration of the H α filament and X-ray sigmoid in NOAA AR 8151, *Astron. Astrophys.*, **425**, 345–352.
- Sakurai, T. (1981), Calculation of force-free magnetic field with non-constant α , *Solar Phys.*, **69**, 343–359.
- Schrijver, C. J., M. L. Derosa, T. R. Metcalf, Y. Liu, J. McTier-nan, S. Régner, G. Valori, M. S. Wheatland, and T. Wiegelmann (2006), Nonlinear force-free modeling of coronal magnetic fields part I: a quantitative comparison of methods, *Solar Phys.*, **235**, 161–190.
- Schwenn, R. (2006), Space weather: the solar perspective, *Living Rev. Solar Phys.*, **3**, 2. URL: <http://www.livingreviews.org/lrsp-2006-2>.
- Shibata, K., S. Masuda, M. Shimojo, H. Hara, T. Yokoyama, S. Tsuneta, T. Kosugi, and Y. Ogawara (1995), Hot-plasma ejections associated with compact-loop solar flares, *Astrophys. J.*, **451**, L83–L85.
- Song, M. T., C. Fang, Y. H. Tang, S. T. Wu, and Y. A. Zhang (2006), A new and fast way to reconstruct a nonlinear force-free field in the solar corona, *Astrophys. J.*, **649**, 1084–1092.

- Tsuneta, S. (1996), Structure and dynamics of magnetic reconnection in a solar flare, *Astrophys. J.*, *456*, 840–849.
- Valori, G., B. Kliem, and R. Keppens (2005) Extrapolation of a nonlinear force-free field containing a highly twisted magnetic loop, *Astron. Astrophys.*, *433*, 335–347.
- Wang H. N., and T. Sakurai (1998), Cross-section variations of coronal magnetic loops, *Publications of the Astronomical Society of Japan*, *50*, 111–123.
- Wang, H. N., Y. H. Yan, T. Sakurai, and M. Zhang (2000), Topology of magnetic field and coronal heating in solar active regions, II. the role of quasi-separatrix layers, *Solar Phys.*, *197*, 263–273.
- Wang, H. N., Y. Yan, and T. Sakurai (2001), Topology of magnetic field and coronal heating in solar active regions, *Solar Phys.*, *201*, 323–336.
- Wheatland, M. S. (2006), A fast current-field iteration method for calculating nonlinear force-free fields, *Solar Phys.*, *238*, 29–39.
- Wheatland, M. S., P. A. Sturrock, and G. Roumeliotis (2000), An optimization approach to reconstructing force-free fields, *Astrophys. J.*, *540*, 1150–1155.
- Wiegelmann, T. (2004), Optimization code with weighting function for the reconstruction of coronal magnetic fields, *Solar Phys.*, *219*, 87–108.
- Wiegelmann, T., B. Inhester, and T. Sakurai (2006), Preprocessing of vector magnetograph data for a nonlinear force-free magnetic field reconstruction, *Solar Phys.*, *233*, 215–232.
- Yan, Y. (2005), On the coronal magnetic field configuration and solar flare/CME process, *Space Sci. Rev.*, *121*, 213–221.
- Yan, Y., and Z. Li (2006), Direct boundary integral formulation for solar non-constant- α force-free magnetic fields, *Astrophys. J.*, *638*, 1162–1168.
- Yan, Y., and T. Sakurai (2000), New boundary integral equation representation for finite energy force-free magnetic fields in open space above the sun, *Solar Phys.*, *195*, 89–109.

H. He, and H. N. Wang, National Astronomical Observatories, Chinese Academy of Sciences, 20A Datun Road, Chaoyang District, Beijing 100012, China. (hehan@bao.ac.cn; hnwang@bao.ac.cn)